Published in final edited form as:
Biochim Biophys Acta. 2012 December ; 1818(12): 3121–3130. doi:10.1016/j.bbamem.2012.08.012.

Probing Ion Channel Activity of Human Islet Amyloid Polypeptide (Amylin)

Jun Zhao[1], **Yin Luo**[1,2], **Hyunbum Jang**[3], **Xiang Yu**[1], **Guanghong Wei**[2], **Ruth Nussinov**[3,4,*], and **Jie Zheng**[1,*]

[1]Department of Chemical and Biomolecular Engineering, The University of Akron Akron, Ohio 44325

[2]State Key Laboratory of Surface Physics, Key Laboratory for Computational Physical Sciences (MOE), and Department of Physics, Fudan University, Shanghai, P.R. China

[3]Basic Science Program, SAIC-Frederick, Inc., National Cancer Institute, Center for Cancer Research Nanobiology Program, Frederick National Laboratory for Cancer Research, Frederick, Maryland 21702

[4]Sackler Inst. of Molecular Medicine Department of Human Genetics and Molecular Medicine Sackler School of Medicine, Tel Aviv University, Tel Aviv 69978, Israel

Abstract

Interactions of human islet amyloid polypeptide (hIAPP or amylin) with the cell membrane are correlated with the dysfunction and death of pancreatic islet β-cells in type II diabetes. Formation of receptor-independent channels by hIAPP in membrane is regarded as one of the membrane-damaging mechanisms that induce ion homeostasis and toxicity in islet β-cells. Here, we investigate the dynamic structure, ion conductivity, and membrane interactions of hIAPP channels in the DOPC bilayer using molecular modeling and molecular dynamics simulations. We use the NMR-derived β-strand-turn-β-strand motif as a building block to computationally construct a series of annular-like hIAPP structures with different sizes and topologies. In the simulated lipid environments, the channels lose their initial continuous β-sheet network and break into oligomeric subunits, which are still loosely associated to form heterogeneous channel conformations. The channels' shapes, morphologies and dimensions are compatible with the doughnut-like images obtained by atomic force microscopy, and with those of modeled channels for Aβ, the β_2-microglobulin-derived K3 peptides, and the β-hairpin-based channels of antimicrobial peptide PG-1. Further, all channels induce directional permeability of multiple ions across the bilayers from the lower to the upper leaflet. This similarity suggests that loosely-associated β-structure motifs can be a general feature of toxic, unregulated channels. In the absence of experimental high-resolution atomic structures of hIAPP channels in the membrane, this study represents a first attempt to delineate some of the main structural features of the hIAPP channels, for a better understanding of the origin of amyloid toxicity and the development of pharmaceutical agents.

*To whom correspondence should be addressed: ruthnu@helix.nih.gov and zhengj@uakron.edu.

Keywords

hIAPP; ion channel; directional permeability; molecular dynamics

Introduction

Human islet amyloid polypeptide (hIAPP or amylin), a 37-residue hormone peptide, is synthesized and secreted together with insulin by the pancreatic islet β-cells [1]. The normal physiological functions of hIAPP as hormone are to regulate gastric emptying, suppress food intake, and control glucose homeostasis [2, 3]. When hIAPP peptides misfold and self-assemble into β-sheet-rich aggregates upon interacting with cell membrane, they can cause the death of β-cells, which is pathologically linked to insulin secretion in type II diabetes [4]. Increasing evidence suggests that small, dynamic, transient, and heterogeneous hIAPP oligomers are more toxic to β-cells than monomers and fibrils. Several hIAPP oligomeric and fibrillar structures have been determined computationally and experimentally, including linear fibrils by solid-state NMR [5], annular aggregates by AFM [6], and linear, annular, and triangular structures predicted by molecular simulations [7, 8]. Although the toxicity of hIAPP aggregates is very likely to be related to membrane disruption, the exact mechanism remains elusive [9, 10].

hIAPP peptides can interact with membranes to introduce membrane disruption via different mechanisms (i.e. receptor-dependent, ion channel, membrane detergent-like, and membrane thinning/curvature models). hIAPP can interact with a number of membrane receptors such as G-protein-coupled receptor, RAMPs, CT receptor [11, 12], amylin receptor [13], and the mechanosensitive calcium channel TRPV4 [14]. Misfolded hIAPP oligomers can also bind to membrane receptors. Unlike the traditional detergent-like model for membrane fragmentation that general requires higher peptide/lipid ratios above a threshold value, IAPP peptides fragment membranes at lower peptide/lipid ratios, while suppressing membrane fragmentation at higher peptide/lipid ratios [15]. This suggests that at lower concentration, hIAPP peptides tend to form intermediate oligomers, which could be bypassed to undergo alternative pathway at higher concentration. hIAPP peptides can directly insert into the cell membrane to form receptor-independent channels, which allow ions and water to cross the membrane and thus to induce abnormal ion homeostasis and oxidative stress [16]. It is also likely that hIAPP peptides form pores by inducing excessive curvature in the membrane [17]. Various ion-permeable channels formed by hIAPP [6, 18], Aβ [19–21], and the K3 peptides, derived from β_2-microglobulin [22, 23] have been visualized and characterized by atomic force microscopy (AFM), electrophysiology, cell calcium imaging, and molecular dynamics (MD) simulations. Aβ channels exhibited Ca^{2+}-selective ion-permeable characteristics [24–27], while K3 [22, 28] and hIAPP [6, 18] formed relatively nonselective, voltage independent, ion-permeable channels in phospholipid bilayer membranes. Different ion conductivity and selectivity of these amyloid channels could be attributed to the variability in peptide sequence and composition, sidechain packing and backbone conformation, and channel topology.

Unlike gated transmembrane ion channels such as gramicidin, which have a precise structure and mechanism to control channel conformations between the open and close states for selective transportation of specific ions across the membrane, amyloid ion channels in the cell membrane appear to consist of several loosely contacting mobile subunits, with certain extent of β-sheet structures. Such dynamic and irregular channels formed by amyloid peptides allow heterogeneous ion permeability. More importantly, recent studies have highlighted the striking resemblance in channel structure and activity of amyloid peptides to other ion channels formed by antimicrobial peptide and toxin proteins. NMR reveals that

Aβ, K3, and hIAPP fibrils adopt U-shaped, β-strand-turn-β-strand structures, and recent MD simulations further confirm that such U-shaped conformations of Aβ and K3 are able to assemble into channel structures in the lipid bilayers. To further explore whether a U-shaped conformation could be a generic structural motif for amyloid channels, we use a β-strand-turn-β-strand hIAPP monomer derived from hIAPP fibrillar structures by NMR [5] to computationally model a series of hIAPP ion channels with different numbers of peptides (12-mer, 18-mer, 24-mer, and 36-mer), channel sizes (2 – 4 nm inner diameter and 7–9 nm outer diameter), and channel topology (CN*p*NC channels: N-terminal β-strands facing the solvated pore and C-terminal β-strands interacting with lipids; and NC*p*CN channels: C-terminal β-strands facing the solvated pore and N-terminal β-strands interacting with lipids) in the zwitterionic lipid bilayer containing 1,2-dioleoyl-sn-glycero-3-phosphocholine (DOPC). Simulation results show that U-shaped hIAPP peptides form channel-like structures assembled by 3–5 dynamically associated subunits, in line with AFM images and other, Aβ and K3, amyloid channels. The potential of mean force (PMF) indicates that both CN*p*NC and NC*p*CN channels of 12–36 peptides induce multiple ion conductivity along the same direction from the lower bilayer leaflet to the upper bilayer leaflet. Comparison of the hIAPP channels with those other β-sheet amyloid channels shows that all modeled channels share structural features including subunit morphology, ion conductivity, and preferential pore sizes.

Materials and Methods

The monomeric structure of the $hIAPP_{1–37}$ peptide was extracted and averaged from 10 solid-state NMR-derived structures from Tycko's lab [5]. Each $hIAPP_{1–37}$ monomer had a U-bent structure consisting of two β-strands connected by a loop, i.e. β-strand(Lys1-Val17)-loop(His18-Leu27)-β-strand(Ser28-Tyr37). Similar turn conformations centered on Phe23, Gly24, and Ala25 were also obtained in SDS micelles by solution NMR [29] and in vacuum MD simulations [30]. The intra-molecular disulfide bond between Cys2 and Cys7 stabilizes the structure at the N-terminus. The N- and C-termini were blocked by NH_3^+ and COO^- groups, respectively. Note that physiologically expressed IAPP has an amidated C-terminus while the structures of membrane bound hIAPP monomers in detergent micelles show some differences between the amidated and non-amidated forms [31, 32]. How these termini forms affect the oligomer and fiber structure is unknown. To construct the β-sheet channel, a single hIAPP monomer was taken as a building block, replicated and rotated along the channel axis to build a circular channel-like structure. Channel sizes can be tuned using a varying number of monomers, and initial separation distance between peptides and the axis center. The channel structures were then minimized with a rigid body motion for the peptides to enhance the formation of intermolecular backbone hydrogen bonds between β-strands, followed by the insertion of the channels into the DOPC bilayer using the CHARMM-GUI membrane builder generator [33]. DOPC lipids were randomly selected from a lipid library and assembled around the channel to satisfy a per lipid surface area of ~72.5$Å^2$ at 300 K [34]. The resulting systems were solvated by TIP3P water molecules, and KCl, NaCl, and $CaCl_2$ at the same concentration were added to neutralize the system and to achieve a total concentration of ~210–260 mM.

In the equilibration stage, each system was gradually relaxed by performing a series of dynamic cycles, in which the harmonic restraints on peptides in the channels were gradually removed to optimize the peptide-lipid and peptide-water interactions. In the production stage, all simulations were performed using the NPAT (constant number of atoms, pressure, surface area, and temperature) ensemble at 300 K. The surface area in the *xy* plane was kept constant while allowing a volume change in the z direction. The van der Waals (vdW) interactions were calculated using a switch function with a twin-range cutoff at 12 and 14 Å. Long-range electrostatic interactions were calculated using the Particle Mesh Ewald (PME)

method. Each hIAPP-lipid system was repeated twice using the same channel configuration, different lipid conformations randomly selected from the lipid library, different initial velocities for all atoms. All MD simulations were performed using the NAMD software [35] with CHARMM27 force field [36]. MD trajectories were saved by every 2 ps for analysis. A summary of all simulation systems was listed in Table S1 (see supplementary material).

Results and Discussion

Heterogeneous and dynamic hIAPP channel structures

Visual inspection of the MD trajectories showed that all hIAPP channels lost their initial perfect circular shape and gradually transited into several subunits, which loosely contacted with each other to form a pore-like structure (Figure S1). Backbone root-mean-square deviations (RMSDs) of the NC*p*CN and CN*p*NC channels reached relatively stable plateaus after 30-ns MD simulations, suggesting that the channels are fully relaxed in the lipid bilayer. The β-sheet population of the individual peptide was used to measure the discontinuous β-sheet network and to determine the number of subunits (Figure 1 and Figure S2). Due to the small size and low β-sheet population of the 12-mer, there was no obvious clustering effect for both CN*p*NC and NC*p*CN 12-mer channels. The 18-mer NC*p*CN and CN*p*NC channels had triangular shape with three subunits and the 24-mer channels had rectangular shape with four subunits. The 36-mer channels had relatively smaller curvature, with less discontinuous β-sheet network, but they still tended to break into 4–5 ordered subunits. Due to the highly populated β-sheets in the 36-mer channels, hIAPP peptides tended to form fibril-like structures. High-resolution AFM images also revealed that the pore-like structures were composed of 4–5 subunits in the DOPC bilayer [6], in agreement with the modeled hIAPP channels. Other amyloid pores in the lipid bilayer obtained from AFM and MD simulations [19–21, 23, 37, 38] typically consist of 3–7 loosely associated mobile subunits, depending on peptide sequences and their interactions with the surroundings. We suggest that dynamic assembly of several subunits into an amyloid pore is a generic structural feature of amyloid pores.

The averaged pore structures were calculated using the HOLE program [39]. In Figures 2 and S3, the degree of the pore diameters was indicated by the color in the order of red < green < blue. For the CN*p*NC channels, pore/outer diameters were 1.5/5.1, 1.8/6.2, 2.1/6.9, and 3.5/7.8 nm for 12-mer, 18-mer, 24-mer, and 36-mer, respectively. The NC*p*CN channels had similar pore and outer diameters to those CN*p*NC channels, i.e. pore/outer diameters were 0.8/5.0, 1.7/6.3, 2.0/7.1, and 3.6/8.2 nm for 12-mer, 18-mer, 24-mer, and 36-mer, respectively. All channels remained open, but the 12-mer channels had more tortuous pore structure than the intermediate 18-, 24-, and 36-mer channels. Recent AFM images [6] showed that the pore and outer diameters of the hIAPP channels were 1–2 nm and 7–12 nm, respectively, consistent with our 18-mer and 24-mer channels (pore: 1.7–2.1 nm and outer: 6.2–7.1 nm). As compared to the AFM values, the outer diameters of the 12-mer channels (5.0~5.1 nm) were too small, while the pore diameters of the 36-mer channels (3.5–3.9 nm) were too large. Thus, the 18-mer and 24-mer channels appear to be the more likely structures in the lipid bilayer.

In the initial energy-minimized channel structures, both pore-facing and lipid-contacting β-strands contained a large population of β-structure. As the simulations proceeded, all channels gradually relaxed in the lipid bilayer, causing the loss of β-structure to some extent. The averaged β-structure percentages over the last 10-ns simulations, calculated by the DSSP algorithm in VMD [40, 41], were ~10% for 12-mer, 25%~27% for 18-mer, 37%~43% for 24-mer, and 47%~50% for 36-mer (Figure S4). The intermediate NC*p*CN channels (18-, 24-, and 36-mer) had slightly higher β-structure population than those of CN*p*NC channels, because the hydrophobic match between the N-terminal hydrophobic

residues near the loop and lipid tails maintained the stability of the β-sheet in the NC*p*CN channels. In contrast, in the CN*p*NC channels the positively charged N-terminal residues of Lys1 and Arg11 induced the larger electrostatic repulsion when they were packed towards the pore. Nevertheless, in general, the pore-facing β-strands were well maintained in all cases, while the lipid-contacting β-strands lost their β-structures to some extent because the larger curvature and separation distance at the channel periphery prevents neighboring peptides from forming intermolecular backbone hydrogen bonds to stabilize β-structure.

PMF for ion binding to hIAPP channels

To characterize channel activity, potential of mean force (PMF) was calculated to measure the relative free energy change required to transfer ions from the bulk water phase to water-lipid interface to channel interior along the z axis, using $\Delta G_{PMF} = -k_B T \ln(\rho_Z/\rho_{bulk})$ where k_B is the Boltzman constant, ρ_z is the ion density at position z along the channel axis, and ρ_{bulk} is the ion density in the bulk phase (Figure 3 and Figure S5). A negative (positive) PMF value indicates favorable (unfavorable) interactions of ions with the surrounding, which suggests the high (low) probability for ions across the bilayers.

For the CN*p*NC channels, all PMF curves of Cl^- displayed a similar asymmetrical S-shape, with a negative minimum at 0~−1 nm and a positive maximum at 1~2 nm. The horizontal S-shape PMF curves clearly indicated that Cl^- preferred to enter the hIAPP channels from the lower bilayer leaflet, because Lys1 (−1.7nm) and Arg11 (−0.7nm) near the lower leaflet formed circular clusters, which provide strong attractive force to drive Cl^- into the interior of the solvated pore. Conversely, the hydrophobic Phe15 and Val17 patches (~1.8 nm) near the upper bilayer leaflet created an energy barrier of 1~2 kJ/mol for preventing Cl^- from entering the channels. For the NC*p*CN channels, the amphiphilic C-terminal β-strands, rather than the positively charged N-terminal residues of Lys1 and Arg11, formed the solvated pore. Consequently, the PMF curves of Cl^- showed that the minimal peaks appeared at −1 nm in the CN*p*NC either largely decreased or disappeared, because attractive electrostatic interactions between Cl^- and Lys1/Arg11 residues in the NC*p*CN channels were greatly reduced.

Apart from the PMF of the Cl^- anion, the trends in PMF for Na^+ are qualitatively similar to those observed for K^+ in the CN*p*NC channels of various diameters, showing strong repulsive energy penalty for these ions to bind to the bilayer and to further enter the channels from either side of the DOPC bilayer. Both Na^+ and K^+ displayed similar unfavorable interactions with the NC*p*CN channels, but with lower repulsive energy. Unlike K^+ and Na^+ that exhibit a very low binding probability to the bilayers, Ca^{2+} were highly populated at both bilayer leaflets, as reflected by two minimal peaks at the channel axis of −2~ −3 nm and 2~3 nm in the PMF curves of Ca^{2+}. This fact indicates that Ca^{2+} have favorable interactions with the lipids. Visual inspection of MD trajectories also confirmed that Ca^{2+} tightly bound to both the negatively charged phosphate groups in the DOPC lipid heads and C-terminus of hIAPP peptides. The preferential and dominant binding of Ca^{2+} to the DOPC bilayer largely reduces the possibility for Na^+ and K^+ to bind to or cross the bilayer. The smallest CN*p*NC and NC*p*CN channels (12-mer), which did not collapse, provide ion binding sites at the entry and inner parts of the channels. As the channel size increased to 36-mer, the NC*p*CN channel showed much lower binding resistance to K^+ and Na^+ than the CN*p*NC channel, because the repulsion from the positively charged rings formed by Lys1 and Arg11 were reduced.

Ion permeability of hIAPP channels

Visual inspection of the MD trajectories showed that all hIAPP channels (12-, 18-, 24-, and 36-mer) were able to induce ion permeability. To quantitatively measure the net ion flux/

permeability across the DOPC bilayer, we use a "right-hand rule" to define a positive direction if ions conduct from the lower bilayer leaflet (i.e. Tyr37 for CN*p*NC model and Ala5 for NC*p*CN model in N/C-terminus region of channels) to the upper bilayer leaflet (i.e. Ser20 for both CN*p*NC and NC*p*CN model in U-turn region of channels), and in a negative direction for ion conductivity. Figures 4 and S6 show the net fluxes of ions as a function of time for hIAPP channels with different channel diameters. Simulation results showed that all ions conducted through the hIAPP channels in a positive direction from the lower to the upper bilayer leaflet, although all cations displayed relatively poor directional conductivities. Overall, both CN*p*NC and NC*p*CN channels displayed high selectivity of Cl^- over cations (Ca^{2+}, Na^+, and K^+). The flux of Cl^- was significantly higher than the fluxes of cations in all channels, consistent with the PMF profiles.

Transport of ions through a hIAPP channel is generally governed by two steps: the first approaching the entrance of the channel and the second flowing through the solvated pore. The combination of these two steps results in a net flux. The first step provides a critical control for the ion flux. Positively charged Lys1 and Arg11 (located at the N-terminal of hIAPP in the lower DOPC bilayer leaflet) formed anionic binding sites, which induced favorable electrostatic binding for Cl^-. Once the binding sites were fully occupied by Cl^-, increased repulsive force between Cl^- drove the ions across the channels. In the case of Ca^{2+}, it is observed that Ca^{2+} barely crosses the bilayer in all channels during the 52 ns of MD trajectories. Since Ca^{2+} tightly bound to the phosphate groups of the lipid bilayer as shown in PMF profiles, they exhibited very low mobility, mostly occupying these binding sites for the entire simulation. This fact indicates that strong binding between Ca^{2+} and the lipid bilayer can greatly reduce the ion conductivity across the bilayer. Unlike Ca^{2+}, very few K^+ and Na^+ (< 5 ions) were able to conduct through the channels (Figures 4 and S6). Visual inspection of MD trajectories revealed that K^+ and Na^+ displayed a high mobility within 10 Å of the lipid bilayer, due to lack of binding sites that have been preoccupied by Ca^{2+}. High mobility and thermal fluctuation caused the weak ion conductivity of K^+ and Na^+ through the channels. In particular, those ion conducting events occurred mostly during the first 30-ns of the simulations. Once the systems achieved an equilibrium state, no further K^+ and Na^+ conduction through the bilayer was observed. Thermal fluctuation-driven ion conductivity is similar to the case of conducting water molecules through hydrophobic nanotubes.

Interaction of channels with their environment

Interaction of channel peptides with lipids and water molecules in the environment plays an important role in supporting the structure and activity of channels. For each channel, we calculated peptide-lipid interaction and peptide-water interaction, averaged over time and the number of peptides in the channels (Figure 5). Overall, all channels had favorable interactions (negative value) with both lipids and water molecules, suggesting that the environment supports channel conformation. For both NC*p*CN and CN*p*NC pore topologies, the 12-, 18-, and 24-mer channels had similar interactions with the lipids, as shown by −120~−140 kcal/mol for the NC*p*CN channels and −100~−110 kcal/mol for the CN*p*NC channels. But, as the channel size increased to 36-mer, the normalized peptide-lipid interactions were significantly reduced to −45 kcal/mol for the CN*p*NC channel and −40 kcal/mol for the NC*p*CN channel. As compared to the subunits in the 12- to 24-mer channels, the subunits in the 36-mer channels appeared to be more rigid because they contained a relatively larger number of peptides with a high population of β-structure (47%~50%). Thus, the rigid subunits had lower flexibility to adapt their conformations to interact with lipids. The less favorable interactions for the 36-mer further support the conclusion that the 36-mer channel structures are unlikely to be lipid-supporting channels, consistent with AFM images. The NC*p*CN channels interacted more strongly with the lipids

than the CN*p*NC channels (except the largest 36-mer channels). Both N- and C-terminal β-strands contributed hydrophobic match near the loop (i.e. Leu12-Val17 in the N-terminal β-strand and Phe23-Leu27 in the C-terminal β-strand) interacting with the lipids. Since the C-terminal residues of 20–29 (SNNFGAILSS) have been shown to be critical for amyloid formation [42], packing of the C-terminal β-strands towards the pore preserved the intermolecular backbone hydrogen bonds, which help to stabilize an inner β-sheet and retain peptide association. Meanwhile, the lipid-contacting N-terminal β-strands carrying two positively charged residues, Lys1 and Arg11, in the NC*p*CN channels strongly interact with lipid headgroups in the lower bilayer leaflet, reducing electrostatic repulsion as compared to the pore-facing N-terminal β-strands in the CN*p*NC channels. Both effects produce more favorable interactions of the NC*p*CN channels with the lipids. Decomposed energy contributions (i.e., vdW and electrostatic interactions) further revealed that the NC*p*CN channels were stabilized by comparable 39.9–49.1% vdW and ~51.7%–60.1% electrostatic interactions, whereas the CN*p*NC channels were mainly stabilized by vdW interactions of 61.2–70.3%. Large differences in energy contribution indicate that different packing between lipids and peptides lead to different vdW and electrostatic contributions in each case.

Visual inspection of MD trajectories showed that all hIAPP channels were well hydrated, including a central water pore and a hydrated cavity inside the U-shape turns. The averaged peptide-water interactions for the CN*p*NC/NC*p*NC channels were −798.2/−762.1, −801.0/−710.9, −645.6/−603.3, −473.6/−455.2 kcal/mol for 12-mer, 18-mer, 24-mer, and 36-mer, respectively. The interactions of the CN*p*NC channels with water molecules were slightly stronger than those of the NC*p*CN channels. The 36-mer channels had relatively weak peptide-water interactions. The subunits of the 36-mer channels presented ordered β-strand packing with fully saturated hydrogen bonds between peptides, which prevents hydrogen bond formation between the peptides and water molecules. Peptide-water interactions were much stronger than peptide-lipid interactions, suggesting that unbalanced interactions could be attributed to the channel breaking into several subunits.

Structure and dynamics of lipid bilayers

To characterize the perturbation effects of hIAPP channels on the lipid ordering, we calculate the deuterium order parameter S_{CD}, using $S_{CD} = 0.5\langle 3\cos^2 \theta_{ij} - 1\rangle$ where θ_{ij} is the angle between the C–H vector and the bilayer normal and the angular bracket represents averaging over lipids and over time. Figure S7 compares the averaged S_{CD} of two oleoyl acyl chains for various carbon atoms in all simulated channel systems. The S_{CD} values of pure DOPC lipids without hIAPP channels were also calculated for comparison. Higher S_{CD} value indicates more ordered lipid chains. It can be seen that the S_{CD} values of lipids for all channel systems were smaller than those in a pure DOPC bilayer, suggesting that the membrane-embedded hIAPP channels affect the ordering of lipid chains. The shapes of S_{CD} curves were similar for all channel systems, but displayed different extent of lipid ordering, which strongly depends on the local interactions between lipids and channels.

To further quantify whether the amyloid channel induces membrane thinning, we measured the thickness and curvature of the lipid bilayer by projecting phosphorus atoms of the lipid headgroups onto the *xz* plane (Figures 6 and S8). The bilayer thickness is measured by the distance between the average positions of the phosphorus atoms in each leaflet, while the bilayer curvature is quantified by the positions of the phosphorus atoms in each leaflet. In all starting configurations, the bilayer thicknesses measured by the phosphate–phosphate distance between two leaflets was 40.2 Å and the bilayer surfaces were flat. Figure 6 shows that for all channel systems, the channel peptides moderately depressed the local bilayer by ~3–5 Å as compared to the starting configurations, forming minor grooves beneath the peptides. The non-peptide contact bilayers remained flat with undisturbed thickness of 40.2

Å at a distance of ~25–42 Å from the center of channels. This fact indicates that bilayer thinning is very localized, and only confined to the peptide–lipid contact region, especially at the two peptide termini. The degree of the bilayer thinning effect appears not to be correlated with the size and topology of the channels. Instead, peptide insertion depth and buried peptide sequence could play key roles in local bilayer thinning. Similar local bilayer distortion behavior was also reported for other pore-forming peptides [43, 44]. While not addressed here, other components of cell membranes such as cholesterol, membrane proteins, and protein receptors play an important role in regulating peptide conformation, adsorption, and aggregation, and thus in biological function and the dynamic structure of cell membranes, and in hIAPP-lipid interactions. Jha et al. [45] and Weise et al. [46] have reported that in the raft membrane containing enriched sphingolipids and cholesterol, hIAPP aggregates faster and exhibits a much higher propensity for fibrillation than in the pure lipid bilayer. Wakabayashi et al. [47] also clearly showed that hIAPP rapidly accumulated in ganglioside- and cholesterol-rich microscopic domains (i.e. lipid-raft domain), and depletion of gangliosides or cholesterol significantly reduced the amount of amyloid deposits. The results of these studies are also in line with our recent computational work [48], showing that increased cholesterol level in lipid bilayer promotes the association of Aβ42 monomer with the POPC bilayer.

Comparison with other amyloid channels

Numerous studies have shown that amyloid peptides can insert into the membrane to form receptor-independent channels as shown by a series of AFM images [6, 20, 49]. Amyloid channels formed by different peptides share common structural characteristics despite the sequence variability (Figure 7). They consist of multiple dynamic subunits, which are loosely associated to form heterogeneous channel-like structures. The size and shape of channels in the membrane vary, but the membrane-supported amyloid channels, which typically appear to have an averaged pore diameter of 1~2 nm and outer diameter of 8~12 nm [6], are wide enough for conducting ions and water to cross the membrane. Interestingly, some antimicrobial peptides such as protegrin-1 (PG-1) can also form channel-like structures in the cell membrane [37], with loosely associated subunits. Thus, such ion-permeable channels may represent a general class of toxic channels, which differ from the natively folded, gated ion-selective channels regulated by two, open and closed states.

Aβ CN*p*NC channels formed by different fragments of $A\beta_{9–42}$, $A\beta_{11–42}$, and $A\beta_{17–42}$ display strong Ca^{2+} binding, in addition to other cations, because the negatively charged Glu22 sidechains near the upper lipid leaflet provide the relative low free energy barriers for Ca^{2+} to bind to and conduct through the channel. K3 (a β_2-microglobulin fragment) forms the NC*p*CN channel-like structures in a DOPC bilayer as observed by modeling and AFM. Electrophysiology studies show that K3 channels permeate multiple ions across the bilayer, with weak cation selectivity, because of an excess of negatively charged groups (Asp34, Glu36, and Asp28) in or near the channel. Our modeled hIAPP channels with different sizes (12- to 36-mer) exhibit highly directional permeability of Cl^- ions and induce strong binding to Ca^{2+} ions. For all modeled Aβ, K3, and hIAPP channels, the U-shaped channel-forming peptides adopt parallel β-sheet arrangement with a “turn-to-tail” orientation, in which the U-turn regions of the peptides located at the upper bilayer leaflet, while the N-/C-terminus locate at the lower bilayer leaflet. However, this may not be the case for other amyloid channels. It is likely that if amyloid peptides insert into the membrane via the U-turn residues first, they can adopt “tail-to-turn” orientation to form a channel with the N-/C-terminus at the upper bilayer leaflet and the turn at the lower bilayer leaflet. Coexistence of “turn-to-tail” and “tail-to-turn” channels in the membrane and their relative populations determine the overall ion conductivity and selectivity. α-helical hIAPP channel structures

have also been proposed [50–52], although it is unclear if membrane disruption involves a channel-like mechanism or non-specific disruption of the membrane [51, 53].

Chang and co-workers [54] used MD simulations to study the structure and dynamics of the modeled β-barrel structures formed by $A\beta_{25–35}$ octamers in the POPG bilayer. They found that these Aβ-barrel channel-like structures adopted a highly populated "in-register mixed parallel-antiparallel" organization, which caused local disturbance of the bilayer and water molecules to pass through. Shafrir et al. [55] reported a computational study showing that six $A\beta_{42}$ peptides can form stable annular β-barrel pore structures in both bulk water and membrane environments. For the proposed β-barrel structures, hydrophobic and glycine residues of Gly29-Ala42 formed a central hydrophobic pore, while hydrophilic N-terminal residues of Asp1-His14 were wrapped around a central core to form a soluble and protective shield. This study did not provide detailed information about the channel activity. Due to a complex energy landscape of polymorphic amyloid oligomers, some experimental structures of Aβ oligomers in solution show a similar subunit structure as the fiber [56, 57], while the subunit structures in others are different [58, 59].

To examine whether hIAPP peptides can penetrate the lipid bilayer via the turn region or the N/C-terminal region with further self-assembly into "turn-to-tail" and "tail-to-turn" channels, we applied steered MD and umbrella sampling to explore the possibility of single hIAPP penetration into the bilayer via different orientations. The penetrating process of amyloid oligomers across the membrane is complicated due to various adsorption orientations of amyloid oligomers on surfaces [60]. Thus, to facilitate peptide penetration across the bilayer and to obtain consensus PMF profiles, three different external forces of 125, 130, and 135 kJ/mol nm^2 were applied to either turn region (Asn21) or tail region (Lys1 and Tyr37), depending on the initial peptide orientation, to pull the peptide across the bilayer. In a single PMF profile, the total separation distance between the center of mass of peptides and the center of the bilayer was divided into 30 windows of 0.2 nm each. In each window we used a different initial configuration, with the peptide left free to rotate around their restrained center of mass at a certain distance from the center of the bilayer. Each point in the PMF profiles requires 100 nanoseconds for equilibration. To obtain the unbiased PMFs, we applied the weighted histogram analysis method (WHAM) [61] using the g_wham [62] module in the GROMACS. Figure 8 presents the PMFs for the transfer of single hIAPP peptide from bulk water to water-bilayer interface to the center of a bilayer. Depending on the insertion orientation, the PMF profiles displayed completely different insertion behaviors. By pulling the tail of hIAPP into the bilayer, the hIAPP peptide preferred to stay in the interior of the bilayer with the lowest energy minima of −18 kcal/mol at z=2.2 nm, as compared to bulk water phase at z>5 nm. The peptide also had comparable probability to fully insert into the lipid bilayer compared to staying in the bulk water phase. This type of PMF usually indicates that the peptides seem to form a barrel-stave pores [63], consistent with our hIAPP channel models. On the other hand, when inserting hIAPP into the bilayer via the turn region, although the peptide still preferred to be partially inserted into the bilayer, an additional barrier of ~11 kcal/mol needed to be overcome so that the peptide can fully cross the bilayer to form a transmembrane pore. Comparison of the two PMF profiles suggests that a certain preferred orientation of peptide insertion is required in order to form a transmembrane pore; thus hIAPP is more likely to penetrate the bilayer via the tail than via the turn region. On-going studies on the co-existence of "turn-to-tail" and "tail-to-turn" channels in the membrane will provide a more complete picture for ion conductivity and selectivity of hIAPP channels. In parallel to channel-induced membrane disruption by amyloid peptides [56], strong evidence also exists for non-channel like membrane disruption. A number of studies [57–60] show that amyloid peptides can fragment the cell membrane, resulting in non-specific ion leakage.

Conclusions

In this work, we investigate the structure and activity of hIAPP channels in the DOPC lipid bilayer using computational modeling and MD simulations. We construct two types of hIAPP channels, each with different size (12-, 18-, 24-, and 36-mer): CN*p*NC channels with charged N-terminal β-strands facing a solvated pore and NC*p*CN model with C-terminal β-strands facing a solvated pore. During the MD simulations, all channels fragment into three to five oligomeric units that are loosely associated, preserving the channel-like structures in the bilayer. Of particular note, 18-mer and 24-mer channels present similar numbers of oligomeric units and overall dimensions to the channels observed by AFM. The bilayer does not support too small 12-mer channels or too large 36-mer channels, consistent with the Aβ channels (17, 27). Due to the formation of anionic binding sites provided by the positively charged N-terminal residues of Lys1 and Arg11 near the lower DOPC bilayer leaflet, they create an electric potential to drive Cl^- through the solvated pore in the same direction, from the lower leaflet to the upper bilayer leaflet. Cl^- display much stronger binding activity to the hIAPP channel and higher flux across the bilayer than cations. The PMF profile shows that, unlike Na^+ and K^+ that are barely adsorbed on the lipid bilayer, Ca^{2+} bind tightly to phosphate groups in the lipid heads, resulting in poor ion conductivity. Na^+ and K^+ exhibit relatively weak ion fluxes due to thermal fluctuation. More importantly, the hIAPP ion channels highlight the striking resemblance of the structure and ion permeability to other amyloid channels, e.g. loosely associated subunits, universal U-shape β-strand–turn–β-strand structure, receptor-independent ion conductivity, and similar dimensions with pore diameters of 1~2 nm and outer diameters of 8~12 nm, which offer unique insights into the membrane disruption mechanism associated with amyloid toxicity. In addition, the local disorder of the membrane upon peptide insertion, together with the tilting of the lipid head, can cause bilayer thinning near the peptide contact region. All hIAPP channels modeled in this work align the hIAPP in parallel to the lipid bilayer via a “turn-to-tail” orientation. However, the hIAPP could also insert into the membrane via “tail-to-turn” orientation to form a channel which is expected to induce an opposite ion conductivity. Co-existence of both channels with different channel topologies could lead to different channel activities. We will address this issue in our ongoing studies of different combination of two distinct hIAPP channels in the lipid bilayer, which is expected to provide a more complete picture for the activity of hIAPP channels associated with amyloid toxicity. We further emphasize that amyloid conformations are broadly polymorphic in water, and on the membrane. Not surprisingly, this polymorphic landscape is also reflected in channel morphologies in the membrane. We may expect a broad range of variants, including channels forming from on-pathway and off-pathway intermediate oligomerization states. It is conceivable that intermediates can also insert into the membrane and at high concentration assemble into toxic channels.

Supplementary Material

Refer to Web version on PubMed Central for supplementary material.

Acknowledgments

We thank Dr. Robert Tycko for providing the atomic coordinates of the hIAPP decamers. This project has been funded in whole or in part with Federal funds from the Frederick National Laboratory for Cancer Research, National Institutes of Health, under contract HHSN261200800001E. The content of this publication does not necessarily reflect the views or policies of the Department of Health and Human Services, nor does mention of trade names, commercial products or organizations imply endorsement by the US Government. This research was supported [in part] by the Intramural Research Program of NIH, Frederick National Lab, Center for Cancer Research. J.Z. thanks for financial support from NSF grants (CAREER Award CBET-0952624 and CBET-1158447) and a 3M Non-Tenured Faculty Award. G.W. thanks for financial support from National Natural Science Foundation of China (Grant No. 11074047) and Research Fund for the Doctoral Program of Higher

Education of China (RFDP-20100071110006). This study in part utilized a 512-node Anton cluster at The National Resource for Biomedical Supercomputing (NRBSC).

References

1. Khemtémourian L, Killian JA, Höppener JWM, Engel MFM. Recent insights in islet amyloid polypeptide-induced membrane disruption and its role in beta-cell death in type 2 diabetes mellitus. Experimental Diabetes Research. 2008; 2008:1–9.
2. Åkesson B, Panagiotidis G, Westermark P, Lundquist I. Islet amyloid polypeptide inhibits glucagon release and exerts a dual action on insulin release from isolated islets. Regulatory Peptides. 2003; 111:55–60. [PubMed: 12609749]
3. Reda TK, Geliebter A, Pi-Sunyer FX. Amylin, food Intake, and obesity. Obesity. 2002; 10:1087–1091.
4. Haataja L, Gurlo T, Huang CJ, Butler PC. Islet amyloid in type 2 diabetes, and the toxic oligomer hypothesis. Endocr Rev. 2008; 29:303–316. [PubMed: 18314421]
5. Luca S, Yau WM, Leapman R, Tycko R. Peptide conformation and supramolecular organization in amylin fibrils: constraints from solid-state NMR. Biochemistry. 2007; 46:13505–13522. [PubMed: 17979302]
6. Quist A, Doudevski I, Lin H, Azimova R, Ng D, Frangione B, Kagan B, Ghiso J, Lal R. Amyloid ion channels: A common structural link for protein-misfolding disease. PNAS. 2005; 102:10427–10432. [PubMed: 16020533]
7. Zhao J, Yu X, Liang G, Zheng J. Heterogeneous triangular structures of human islet amyloid polypeptide (amylin) with internal hydrophobic cavity and external wrapping morphology reveal the polymorphic nature of amyloid fibrils. Biomacromolecules. 2011; 12:1781–1794. [PubMed: 21428404]
8. Zhao J, Yu X, Liang G, Zheng J. Structural polymorphism of human islet amyloid polypeptide (hIAPP) oligomers highlights the importance of interfacial residue interactions. Biomacromolecules. 2011; 12:210–220. [PubMed: 21158384]
9. Brender JR, Salamekh S, Ramamoorthy A. Membrane Disruption and Early Events in the Aggregation of the Diabetes Related Peptide IAPP from a Molecular Perspective. Accounts Chem Res. 2012; 45:454–462.
10. Hebda JA, Miranker AD. The Interplay of Catalysis and Toxicity by Amyloid Intermediates on Lipid Bilayers: Insights from Type II Diabetes. Annual Review of Biophysics. 2009; 38:125–152.
11. Poyner DR, Sexton PM, Marshall I, Smith DM, Quirion R, Born W, Muff R, Fischer JA, Foord SM. International Union of Pharmacology. XXXII. The mammalian calcitonin gene-related peptides, adrenomedullin, amylin, and calcitonin receptors. Pharmacological Reviews. 2002; 54:233–246. [PubMed: 12037140]
12. Christopoulos G, Perry KJ, Morfis M, Tilakaratne N, Gao YY, Fraser NJ, Main MJ, Foord SM, Sexton PM. Multiple amylin receptors arise from receptor activity-modifying protein interaction with the calcitonin receptor gene product. Molecular Pharmacology. 1999; 56:235–242. [PubMed: 10385705]
13. Jhamandas JH, MacTavish D. beta-Amyloid protein (A beta) and human amylin regulation of apoptotic genes occurs through the amylin receptor. Apoptosis. 2012; 17:37–47. [PubMed: 21947943]
14. Casas S, Novials A, Reimann F, Gomis R, Gribble FM. Calcium elevation in mouse pancreatic beta cells evoked by extracellular human islet amyloid polypeptide involves activation of the mechanosensitive ion channel TRPV4. Diabetologia. 2008; 51:2252–2262. [PubMed: 18751967]
15. Brender JR, Dürr UHN, Heyl D, Budarapu MB, Ramamoorthy A. Membrane fragmentation by an amyloidogenic fragment of human Islet Amyloid Polypeptide detected by solid-state NMR spectroscopy of membrane nanotubes. BBA - Biomembranes. 2007; 1768:2026–2029. [PubMed: 17662957]
16. Butterfield SM, Lashuel HA. Amyloidogenic protein-membrane interactions: mechanistic insight from model systems. Angew Chem Int Ed. 2010; 49:5628–5654.

17. Smith PES, Brender JR, Ramamoorthy A. Induction of negative curvature as a mechanism of cell toxicity by amyloidogenic peptides: the case of islet amyloid polypeptide. J Am Chem Soc. 2009; 131:4470–4478. [PubMed: 19278224]

18. Mirzabekov TA, Lin M-c, Kagan BL. Pore Formation by the Cytotoxic Islet Amyloid Peptide Amylin. Journal of Biological Chemistry. 1996; 271:1988–1992. [PubMed: 8567648]

19. Jang H, Zheng J, Nussinov R. Models of {beta}-amyloid ion-channels in the membrane suggest that channel formation in the bilayer is a dynamic process. Biophys J. 2007; 93:1938–1949. [PubMed: 17526580]

20. Jang H, Zheng J, Lal R, Nussinov R. New structures help the modeling of toxic amyloid-[beta] ion channels. Trends Biochem Sci. 2008; 33:91–100. [PubMed: 18182298]

21. Jang H, Arce FT, Ramachandran S, Capone R, Azimova R, Kagan BL, Nussinov R, Lal R. Truncated beta-amyloid peptide channels provide an alternative mechanism for Alzheimer's Disease and Down syndrome. Proceedings of the National Academy of Sciences of the United States of America. 2010; 107:6538–6543. [PubMed: 20308552]

22. Mustata M, Capone R, Jang H, Arce FT, Ramachandran S, Lal R, Nussinov R. K3 Fragment of Amyloidogenic beta(2)-Microglobulin Forms Ion Channels: Implication for Dialysis Related Amyloidosis. Journal of the American Chemical Society. 2009; 131:14938–14945. [PubMed: 19824733]

23. Jang H, Arce FT, Ramachandran S, Capone R, Lal R, Nussinov R. Structural Convergence Among Diverse, Toxic beta-Sheet Ion Channels. Journal of Physical Chemistry B. 2010; 114:9445–9451.

24. Kawahara M, Kuroda Y. Molecular mechanism of neurodegeneration induced by Alzheimer's [beta]-amyloid protein: channel formation and disruption of calcium homeostasis. Brain Research Bulletin. 2000; 53:389–397. [PubMed: 11136994]

25. Demuro A, Mina E, Kayed R, Milton SC, Parker I, Glabe CG. Calcium dysregulation and membrane disruption as a ubiquitous neurotoxic mechanism of soluble amyloid oligomers. J Biol Chem. 2005; 280:17294–17300. [PubMed: 15722360]

26. Arispe N, Pollard HB, Rojas E. Giant multilevel cation channels formed by Alzheimer disease amyloid beta-protein [Abeta P-(1–40)] in bilayer membranes. PNAS. 1993; 90:10573–10577. [PubMed: 7504270]

27. Lin H, Bhatia R, Lal R. Amyloid {beta} protein forms ion channels: implications for Alzheimer's disease pathophysiology. FASEB J. 2001; 15:2433–2444. [PubMed: 11689468]

28. Hirakura Y, Kagan BL. Pore formation by beta-2-microglobulin: a mechanism for the pathogenesis of dialysis associated amyloidosis. Amyloid. 2001; 8:94–100. [PubMed: 11409039]

29. Mascioni A, Porcelli F, Ilangovan U, Ramamoorthy A, Veglia G. Conformational preferences of the amylin nucleation site in SDS micelles: An NMR study. Biopolymers. 2003; 69:29–41. [PubMed: 12717720]

30. Ilangovan U, Ramamoorthy A. Conformational studies of human islet amyloid peptide using molecular dynamics and simulated annealing methods. Biopolymers. 1998; 45:9–20. [PubMed: 9433183]

31. Nanga RPR, Brender JR, Vivekanandan S, Ramamoorthy A. Structure and membrane orientation of IAPP in its natively amidated form at physiological pH in a membrane environment. Biochimica Et Biophysica Acta-Biomembranes. 2011; 1808:2337–2342.

32. Patil SM, Xu S, Sheftic SR, Alexandrescu AT. Dynamic alpha-Helix Structure of Micelle-bound Human Amylin. Journal of Biological Chemistry. 2009; 284:11982–11991. [PubMed: 19244249]

33. Jo S, Kim T, Im W. Automated Builder and Database of Protein/Membrane Complexes for Molecular Dynamics Simulations. PLoS ONE. 2007; 2:e880. [PubMed: 17849009]

34. Petrache HI, Tristram-Nagle S, Gawrisch K, Harries D, Parsegian VA, Nagle JF. Structure and Fluctuations of Charged Phosphatidylserine Bilayers in the Absence of Salt. Biophysical Journal. 2004; 86:1574–1586. [PubMed: 14990484]

35. Kale L, Skeel R, Bhandarkar M, Brunner R, Gursoy A, Krawetz N, Phillips J, Shinozaki A, Varadarajan K, Schulten K. NAMD2: greater scalability for parallel molecular dynamics. J Comput Phys. 1999; 151:283–312.

36. MacKerell AD, Bashford D, Bellott M, Dunbrack RL, Evanseck JD, Field MJ, Fischer S, Gao J, Guo H, Ha S, Joseph-McCarthy D, Kuchnir L, Kuczera K, Lau FTK, Mattos C, Michnick S, Ngo

T, Nguyen DT, Prodhom B, Reiher WE, Roux B, Schlenkrich M, Smith JC, Stote R, Straub J, Watanabe M, Wiorkiewicz-Kuczera J, Yin D, Karplus M. All-atom empirical potential for molecular modeling and dynamics studies of proteins. J Phys Chem B. 1998; 102:3586–3616.

37. Jang H, Arce FT, Capone R, Ramachandran S, Lal R, Nussinov R. Misfolded Amyloid Ion Channels Present Mobile beta-Sheet Subunits in Contrast to Conventional Ion Channels. Biophysical Journal. 2009; 97:3029–3037. [PubMed: 19948133]
38. Jang H, Ma B, Lal R, Nussinov R. Models of toxic beta-sheet channels of protegrin-1 suggest a common subunit organization motif shared with toxic alzheimer beta-amyloid ion channels. Biophys J. 2008; 95:4631–4642. [PubMed: 18708452]
39. Smart OS, Goodfellow JM, Wallace BA. The pore dimensions of gramicidin A. Biophys J. 1993; 65:2455–2460. [PubMed: 7508762]
40. Humphrey W, Dalke A, Schulten K. VMD - visual molecular dynamics. J Molec Graphics. 1996; 14:33–38.
41. Frishman D, Argos P. Knowledge-based protein secondary structure assignment, Proteins: Structure. Function, and Genetics. 1995; 23:566–579.
42. Westermark P, Engstrom U, Johnson KH, Westermark GT, Betsholtz C. Islet amyloid polypeptide-pinpointing amino acid residues linked to amyloid fibril formation. Proceedings of the National Academy of Sciences of the United States of America. 1990; 87:5036–5040. [PubMed: 2195544]
43. Lee MT, Hung WC, Chen FY, Huang HW. Mechanism and kinetics of pore formation in membranes by water-soluble amphipathic peptides. Proc Natl Acad Sci U S A. 2008; 105:5087–5092. [PubMed: 18375755]
44. Manna M, Mukhopadhyay C. Cause and effect of melittin-induced pore formation: a computational approach. Langmuir. 2009; 25:12235–12242. [PubMed: 19754202]
45. Jha S, Sellin D, Seidel R, Winter R. Amyloidogenic Propensities and Conformational Properties of ProIAPP and IAPP in the Presence of Lipid Bilayer Membranes. Journal of Molecular Biology. 2009; 389:907–920. [PubMed: 19427320]
46. Weise K, Radovan D, Gohlke A, Opitz N, Winter R. Interaction of hIAPP with model raft membranes and pancreatic beta-cells: Cytotoxicity of hIAPP oligomers. ChemBioChem. 2010; 11:1280–1290. [PubMed: 20440729]
47. Wakabayashi M, Matsuzaki K. Ganglioside-induced amyloid formation by human islet amyloid polypeptide in lipid rafts. FEBS Letters. 2009; 583:2854–2858. [PubMed: 19647738]
48. Yu X, Zheng J. Cholesterol promotes the interaction of Alzheimer β-amyloid monomer with lipid bilayer. J Mol Biol. 2012; 421:561–571. [PubMed: 22108168]
49. Lashuel HA, Lansbury PT. Are amyloid diseases caused by protein aggregates that mimic bacterial pore-forming toxins? Quart Rev Biophys. 2006; 39:167–201.
50. Brender JR, Lee EL, Cavitt MA, Gafni A, Steel DG, Ramamoorthy A. Amyloid Fiber Formation and Membrane Disruption are Separate Processes Localized in Two Distinct Regions of IAPP, the Type-2-Diabetes-Related Peptide. Journal of the American Chemical Society. 2008; 130:6424–6429. [PubMed: 18444645]
51. Last NB, Rhoades E, Miranker AD. Islet amyloid polypeptide demonstrates a persistent capacity to disrupt membrane integrity. Proceedings of the National Academy of Sciences of the United States of America. 2011; 108:9460–9465. [PubMed: 21606325]
52. Knight JD, Hebda JA, Miranker AD. Conserved and Cooperative Assembly of Membrane-Bound α-Helical States of Islet Amyloid Polypeptide. Biochemistry. 2006; 45:9496–9508. [PubMed: 16878984]
53. Smith PES, Brender JR, Ramamoorthy A. Induction of Negative Curvature as a Mechanism of Cell Toxicity by Amyloidogenic Peptides: The Case of Islet Amyloid Polypeptide. Journal of the American Chemical Society. 2009; 131:4470–4478. [PubMed: 19278224]
54. Chang Z, Luo Y, Zhang Y, Wei G. Interactions of A beta 25–35 beta-Barrel-like Oligomers with Anionic Lipid Bilayer and Resulting Membrane Leakage: An All-Atom Molecular Dynamics Study. Journal of Physical Chemistry B. 2011; 115:1165–1174.
55. Shafrir Y, Durell SR, Anishkin A, Guy HR. Beta-barrel models of soluble amyloid beta oligomers and annular protofibrils. Proteins-Structure Function and Bioinformatics. 2010; 78:3458–3472.

56. Chimon S, Shaibat MA, Jones CR, Calero DC, Aizezi B, Ishii Y. Evidence of fibril-like [beta]-sheet structures in a neurotoxic amyloid intermediate of Alzheimer's [beta]-amyloid. Nat Struct Mol Biol. 2007; 14:1157–1164. [PubMed: 18059284]
57. Scheidt HA, Morgado I, Rothemund S, Huster D, Fändrich M. Solid-State NMR spectroscopic investigation of Aβ protofibrils: implication of a β-sheet remodeling upon maturation into terminal amyloid fibrils. Ange Chem Inter Ed. 2011; 50:2837–2840.
58. Stroud JC, Liu C, Teng PK, Eisenberg D. Toxic fibrillar oligomers of amyloid-β have cross-β structure. Proc Natl Acad Sci U S A. 2012; 109:7717–7722. [PubMed: 22547798]
59. Sarroukh R, Cerf E, Derclaye S, Dufrêne YF, Goormaghtigh E, Ruysschaert JM, Raussens V. Transformation of amyloid β(1–40) oligomers into fibrils is characterized by a major change in secondary structure. Cell Mol Life Sci. 2011; 68:1429–1438. [PubMed: 20853129]
60. Zhao J, Wang Q, Liang G, Zheng J. Molecular Dynamics Simulations of Low-Ordered Alzheimer beta-Amyloid Oligomers from Dimer to Hexamer on Self-Assembled Monolayers. Langmuir. 2011; 27:14876–14887. [PubMed: 22077332]
61. Kumar S, Rosenberg JM, Bouzida D, Swendsen RH, Kollman PA. THE weighted histogram analysis method for free-energy calculations on biomolecules. I. The method. Journal of Computational Chemistry. 1992; 13:1011–1021.
62. Hub JS, de Groot BL, van der Spoel D. g_wham-A Free Weighted Histogram Analysis Implementation Including Robust Error and Autocorrelation Estimates. Journal of Chemical Theory and Computation. 2010; 6:3713–3720.
63. Gkeka P, Sarkisov L. Interactions of phospholipid bilayers with several classes of amphiphilic α-helical peptides: insights from coarse-grained molecular dynamics simulations. J Phys Chem B. 2009; 114:826–839. [PubMed: 20028006]

Highlights

1. Structure and ion activity of hIAPP channels in DOPC bilayer are studied.
2. hIAPP channels are highly selective for Cl- ion transport.
3. Multiple ion conductivity is directional from lower to upper leaflet of bilayer.
3. Channel morphologies and dimensions are compatible with the experiments.
4. Loosely-associated β-subunits are common structural motifs for amyloid pores.

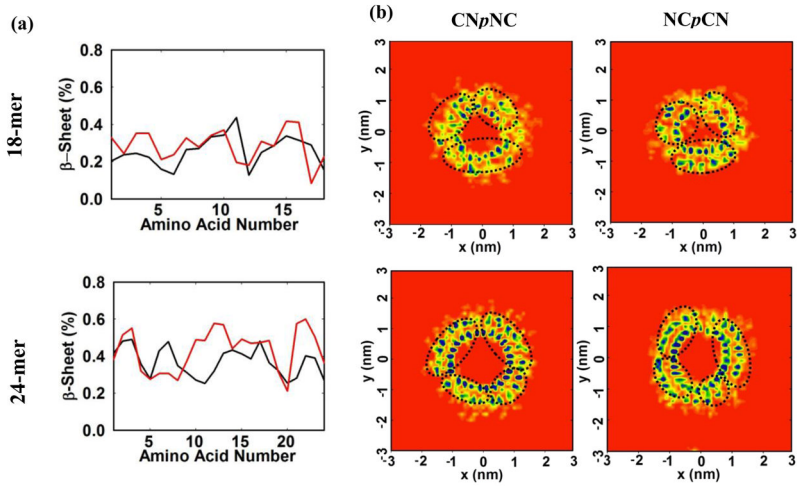

Figure 1.

(a) β-sheet population for 18-mer and 24-mer CN*p*NC channels (*black line*) and NC*p*CN channels (*red line*). (b) Subunit organization for 18-mer and 24-mer CN*p*NC and NC*p*CN channels. Subunits are defined by mapping *x*, *y* coordinates of Cα atoms of hIAPP peptides onto the *x*–*y* plane. The probability to find Cα atoms is represented by an increased color order of *red*, *orange*, *yellow*, *green*, *blue,* and *purple*.

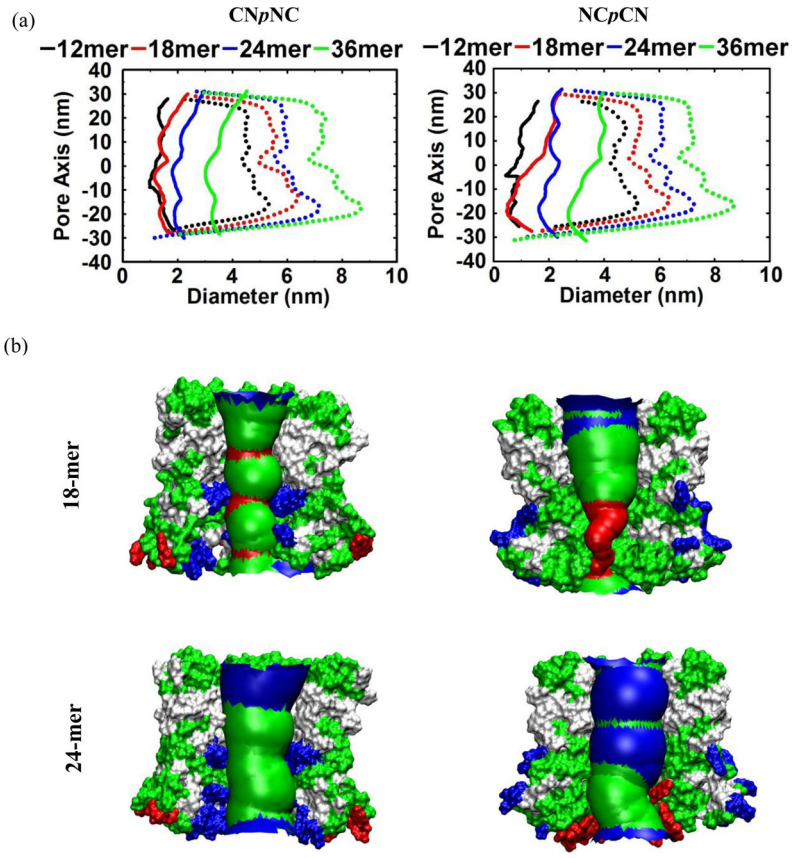

Figure 2.

(a) Averaged pore (solid line) and outer diameters (dashed line) of hIAPP channels and (b) averaged pore structures embedded in the averaged hIAPP channel structures for the 18-mer and 24-mer CN*p*NC and NC*p*CN channels. Average pore diameter along bilayer normal is defined by a red-green-blue scale, with small diameter of <14 Å (*red),* intermediate diameter of 14–16 Å (*green*), and large diameter of > 22 Å (*blue*). Color code for protein: hydrophobic residues (*white*), polar residues (*green*), positively charged residues (*blue*), and negatively charged residues (*red*).

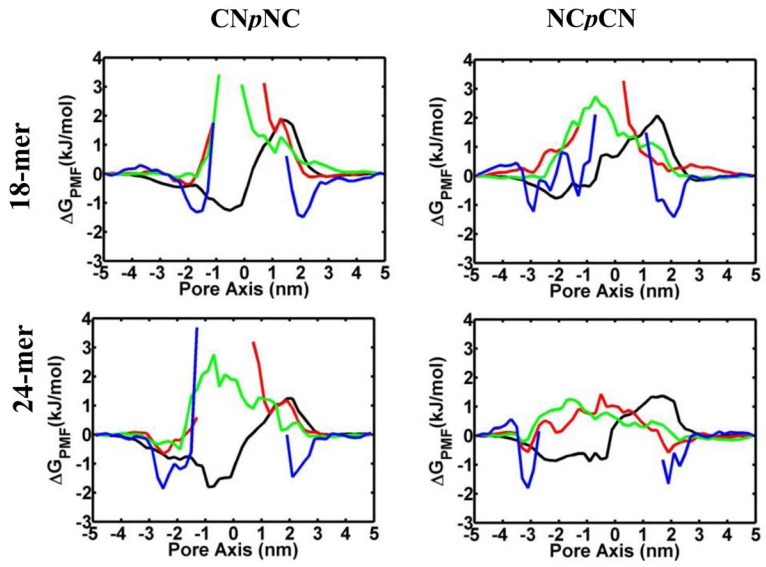

Figure 3.

Potential of mean force (PMF), ΔG_{PMF}, for Cl^- (*black*), Na^+ (*red*), K^+(*green*), and Ca^{2+} (*blue*) as a function of the distance along the channel center axis for the 18- and 24-mer of hIAPP channels. ΔG_{PMF} is calculated using an equation, $-k_B T \ln(\rho_z/\rho_{bulk})$, where k_B is the Boltzmann constant, T is the simulation temperature, ρ_z is the ion density at the position z along the channel axis, and ρ_{bulk} is the ion density in the bulk region.

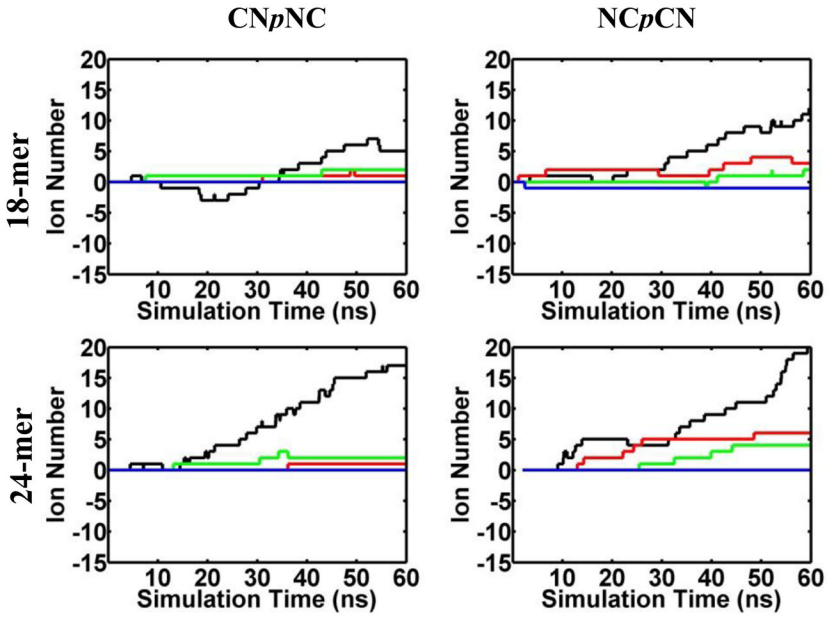

Figure 4.
Net charge flows of Cl^- (*black*), Na^+ (*red*), K^+ (*green*), and Ca^{2+} (*blue*) across the 18-mer and 24-mer channels during the 60-ns MD simulations.

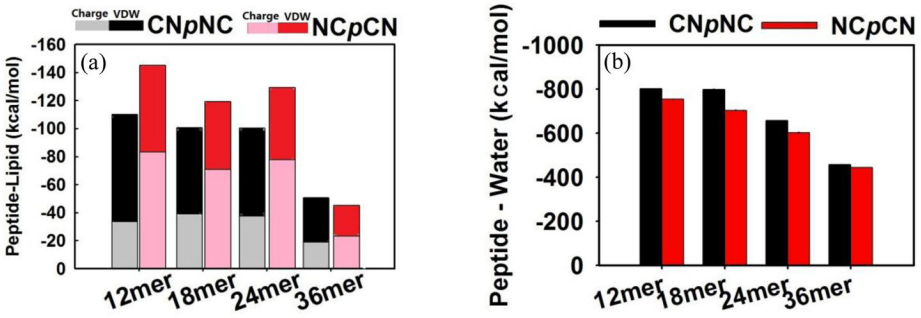

Figure 5.
Interaction energy of channel peptides with (a) DOPC lipids and (b) surrounding water molecules. All interactions energies are normalized by the number of peptides.

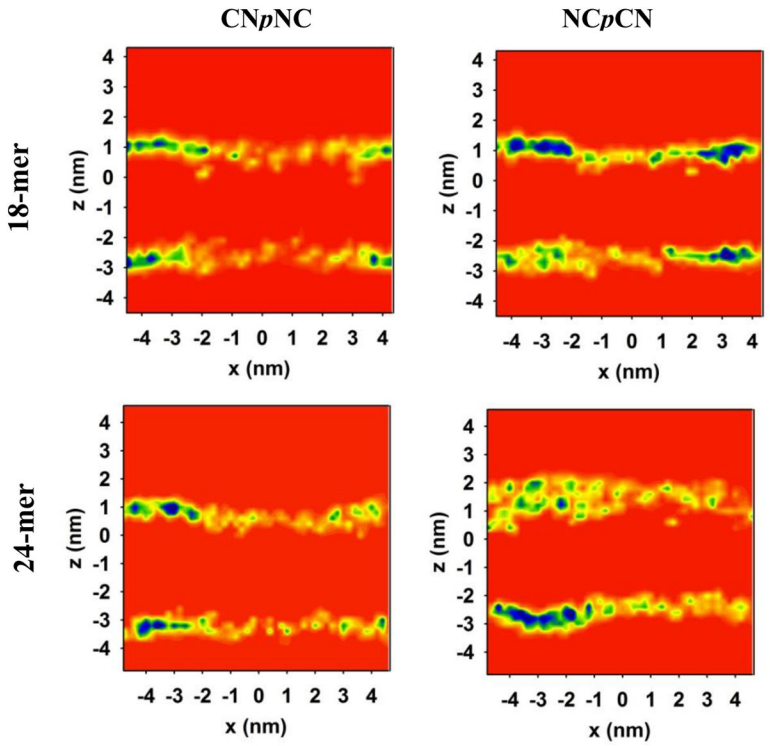

Figure 6.

The bilayer thickness and curvature of 18-mer and 24-mer hIAPP channels, by projecting phosphorus atoms of the lipid headgroups onto the *xz* plane. The probability to find phosphorus atoms is defined by an increased color order of *red*, *orange*, *yellow*, *green*, *blue* and *purple*.

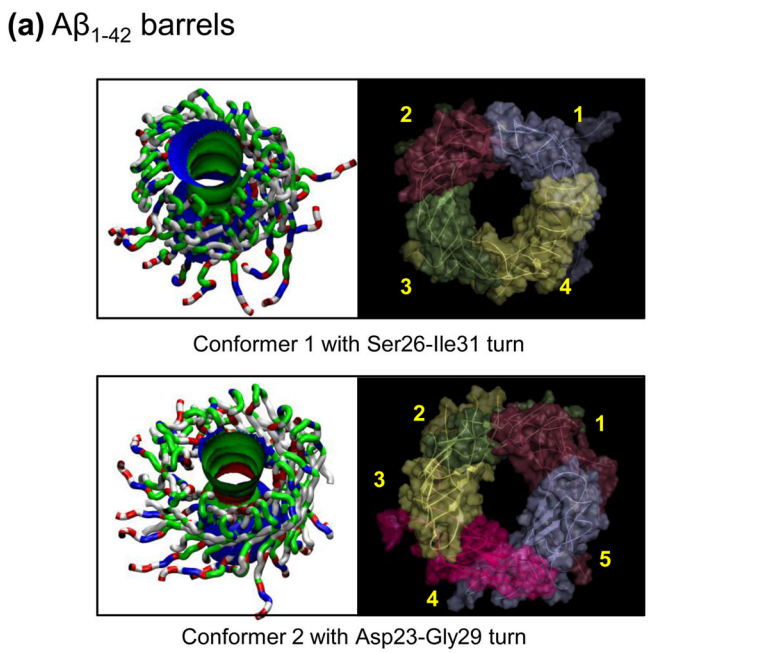

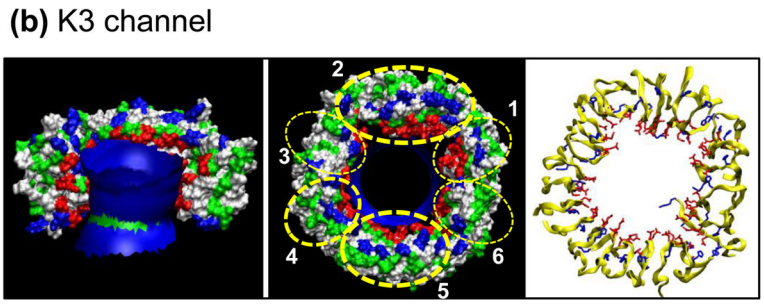

Figure 7.

(a) Averaged pore structures calculated by the HOLE program embedded in the averaged barrel conformations during the simulations for the conformer 1 (turn at Ser26-Ile31) and 2 (turn at Asp23-Gly29) $A\beta_{1-42}$ barrels. In the angle view (left panel) of the pore structure, whole barrel structures are shown with the ribbon representation. The right panel represents the simulated barrel structures with highlighted subunits for the averaged barrels in the surface representation that are shown in the view along the membrane normal. (b) Averaged pore structures embedded in the averaged channel conformations during the simulations for the K3 channel with NC*p*CN topology. In the surface representation for the channel, the front part of the channel in the angle view (left panel) has been removed to allow a view of the pore. In the view along the membrane normal (middle panel), subunits are highlighted by yellow dotted circles. In the right panel, simulated channel structure is shown with the ribbon representation in the view along the membrane normal.

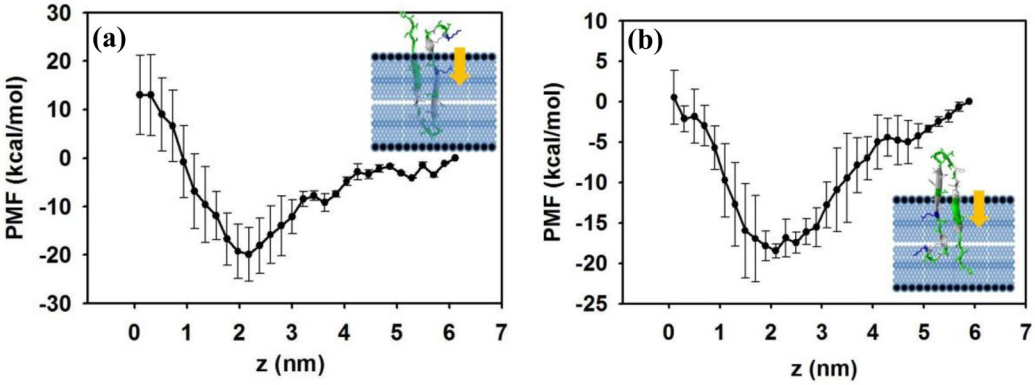

Figure 8.
Potential of mean force (PMF) for the transfer of single hIAPP peptide from bulk water to water-bilayer interface to the center of a bilayer by pulling (a) turn region and (b) tail region into the DOPC bilayer.